



**HAL**  
open science

# A methodology based on the coupled criterion for the assessment of adhesive-to-adherend interface crack initiation

Thiago Birro, Eric Paroissien, Maëlen Aufray, Frederic Lachaud

## ► To cite this version:

Thiago Birro, Eric Paroissien, Maëlen Aufray, Frederic Lachaud. A methodology based on the coupled criterion for the assessment of adhesive-to-adherend interface crack initiation. *International Journal of Adhesion and Adhesives*, 2020, 102, pp.102664-102676. 10.1016/j.ijadhadh.2020.102664 . hal-02877747

**HAL Id: hal-02877747**

**<https://hal.science/hal-02877747>**

Submitted on 22 Jun 2020

**HAL** is a multi-disciplinary open access archive for the deposit and dissemination of scientific research documents, whether they are published or not. The documents may come from teaching and research institutions in France or abroad, or from public or private research centers.

L'archive ouverte pluridisciplinaire **HAL**, est destinée au dépôt et à la diffusion de documents scientifiques de niveau recherche, publiés ou non, émanant des établissements d'enseignement et de recherche français ou étrangers, des laboratoires publics ou privés.



## Open Archive Toulouse Archive Ouverte (OATAO)

OATAO is an open access repository that collects the work of some Toulouse researchers and makes it freely available over the web where possible.

This is an author's version published in: <https://oatao.univ-toulouse.fr/26142>

**Official URL :** <https://doi.org/10.1016/j.ijadhadh.2020.102664>

### To cite this version :

Birro, Thiago and Paroissien, Eric and Aufray, Maëlen and Lachaud, Frédéric A methodology based on the coupled criterion for the assessment of adhesive-to-adherend interface crack initiation. (2020) International Journal of Adhesion and Adhesives, 102. 102664-102676. ISSN 0143-7496

Any correspondence concerning this service should be sent to the repository administrator:

[tech-oatao@listes-diff.inp-toulouse.fr](mailto:tech-oatao@listes-diff.inp-toulouse.fr)

## **A methodology based on the coupled criterion for the assessment of adhesive-to-adherend interface crack initiation**

Thiago V. Birro<sup>1,2</sup>, Eric Paroissien<sup>1\*</sup>, Maëlen Aufray<sup>2</sup>, Frédéric Lachaud<sup>1</sup>

<sup>1</sup> *Institut Clément Ader (ICA), Université de Toulouse, ISAE-SUPAERO, INSA, IMT MINES ALBI, UPS, CNRS, 3 Rue Caroline Aigle, 31400 Toulouse, France*

<sup>2</sup> *CIRIMAT, Université de Toulouse, CNRS, INPT, UPS, 4, allée Émile Monso -BP 44362, 31030 Toulouse Cedex 4, France.*

\*To whom correspondence should be addressed: Tel. +33561338438, E-mail: [eric.paroissien@isae-supero.fr](mailto:eric.paroissien@isae-supero.fr)

**Abstract** – In the framework of lightweight structures, the bonded joints appear as a suitable solution for increasing the mass-to-strength ratio. However, the full understanding of the interface debonding is a key obstacle to be overcome in critical systems. For characterizing adhesive-to-adherend interface crack initiation, the three-point bending test has been shown as a useful test that provides an identifiable small round zone. The samples were manufactured using an aluminum alloy 2024-T3 etched with nitric acid. The adhesive consisted in an epoxy pre-polymer DGEBA, DETA amine and an organosilane GLYMO directly introduced in the mixture. A coupled stress and energy criterion was used for the assessment of the properties of the interfacial debonding, since a stress concentration appears near to the corner of the specimen. For a quick computation, the application of the coupled criterion (CC) used the macro-element technique. On the other hand, most finite-element-based software has already

implemented the cohesive zone modeling (CZM). In this sense, the fracture parameters computed via CC were used for the assessment of cohesive zone modeling of adhesive-to-adherend interface crack initiation. The results of fracture initiation using the CZM showed a good agreement in a macroscale response with the experimental campaign, thus providing a useful tool for a rapid estimation of cracking initiation.

***Keywords:** interface cracking initiation; three-point bending test; coupled criterion; cohesive zone modeling; macro-element;*

## NOMENCLATURE AND UNITS

$a$	crack length (mm)
$a_c$	critical crack length (mm)
$a_{czm}/2$	crack length via CZM (mm)
$a_{min}$	lower crack length (mm)
$a_{max}$	upper crack length (mm)
$A_j$	extensional stiffness (N) of adherend $j$
$b$	width (mm) of the adherends
$b_a$	width (mm) of the adhesive
$b_s$	width (mm) of the substrate
$B_j$	extensional and bending coupling stiffness (N.mm) of the adherend $j$
$d_c$	critical displacement (mm) for three-point bending test
$D$	damage scalar
$D_j$	bending stiffness (N.mm <sup>2</sup> ) of the adherend $j$
$e_a$	interface thickness (mm)
$E_a$	adhesive peel modulus (MPa)
$E_s$	Young's Modulus of the substrate (MPa)
$E_s^*$	equivalent Young's Modulus of the substrate (MPa)
$E_j$	adherend Young's modulus (MPa) of the adherend $j$
$F_c$	critical force (N) of the three-point bending test
$F_e$	element nodal force vector (N)
$G_a$	adhesive shear modulus (MPa)
$G_I$	energy release rate (energy per unit of area: mJ or N/mm) in mode I
$G_{II}$	energy release rate (energy per unit of area: mJ or N/mm) in mode II
$G_{Ic}$	critical energy release rate (energy per unit of area: mJ or N/mm) in mode I

$G_{Ie}$	adhesive elastic energy stored (energy per unit of area: mJ or N/mm) in mode I
$G_{IIc}$	critical energy release rate (energy per unit of area: mJ or N/mm) in mode II
$G_{IIe}$	adhesive elastic energy stored (energy per unit of area: mJ or N/mm) in mode II
$h_a$	thickness (mm) of the adhesive layer
$h_j$	thickness (mm) of the adherend $j$
$h_s$	thickness (mm) of the substrate
$k_I$	interface adjustment stiffness (MPa/mm) in peel
$k_{II}$	interface adjustment stiffness (MPa/mm) in shear
$K_e$	elementary stiffness matrix of a bonded-beam element (N/mm)
$K_{spec}$	global stiffness of the specimen (N/mm)
$k_{yj}$	shear coefficient
$L$	length (mm) of bonded overlap
$L_c$	characteristic fracture length of the interface
$L_{ME}$	overlap length (mm) of a macro-element
$L_{ref}$	overlap length (mm) of a macro-element in the refinement zone
$M_j$	bending moment (N.mm) in adherend $j$ around the $z$ -direction
$M_e$	coupling matrix in terms of nodal loads
$\mathbf{n}$	normal vector to the path
$n_{dam}$	number of completely damaged elements
$n_{proc}$	number of elements of the process zone
$n_{ref}$	number of elements of the refinement zone
$N_e$	coupling matrix in terms of nodal displacements
$N_j$	normal force (N) in adherend $j$ in the $x$ -direction
$s$	curvilinear abscissa (mm)
$S_c$	crack surface (mm <sup>2</sup> ) at the initiation

$T$	traction vector (MPa)
$u_j$	displacement (mm) of adherend $j$ in the $x$ direction
$U_e$	element nodal displacement vector (mm)
$V_j$	shear force (N) in adherend $j$ in the $y$ -direction
$w_j$	displacement (mm) of adherend $j$ in the $y$ -direction
$W$	potential energy (mJ)
$\Delta_j$	characteristic parameter ( $\text{N}^2 \cdot \text{mm}^2$ ) of adherend $j$
$\Delta u$	slipping displacement (mm)
$\Delta w$	opening displacement (mm)
$\alpha$	shear/peel stiffness ratio
$\delta_u$	displacement jump (mm) of the interface along the $x$ -axis
$\delta_{ue}$	displacement jump (mm) of the interface along the $x$ -axis at the initiation
$\delta_{uf}$	displacement jump (mm) of the interface along the $x$ -axis at propagation
$\delta_v$	displacement jump (mm) of the interface along the $y$ -axis
$\delta_{ve}$	displacement jump (mm) of the interface along the $x$ -axis at the initiation
$\delta_{vf}$	displacement jump (mm) of the interface along the $x$ -axis at propagation
$\theta_j$	bending angle (rad) of the adherend $j$ around the $z$ -direction
$\lambda$	norm of displacement jump (mm) of the interface
$\lambda_e$	norm of displacement jump (mm) of the interface at the initiation
$\lambda_f$	norm of displacement jump (mm) of the interface at propagation
$\nu$	Poisson modulus
$\sigma$	interfacial peel stress (MPa)
$\boldsymbol{\sigma}$	stress tensor (MPa)
$\sigma_c$	interfacial tensile stress (MPa)

$\sigma_{eq}$	equivalent stress (MPa)
$\tau$	interfacial shear stress (MPa)
$\tau_c$	critical shear stress (MPa)
$\mathcal{G}$	differential energy release rate (N/mm)
$\mathcal{G}_{inc}$	incremental energy release rate (N/mm)
$\mathcal{G}_c$	fracture toughness (N/mm)
$(x,y,z)$	global reference system of axes (mm)
3PBT	three-point bending test
CC	coupled criterion
CZM	cohesive zone modeling
DOF	degree of freedom
ME	macro-element

## 1. Introduction

Up to now, the bonded assemblies have been used extensively in aeronautical, car manufacturing, construction, and nautical industries to increase the strength-to-mass ratio of lightweight structures. As benefits, the adhesive bonding technology improves fatigue strength, static strength, stiffness, continuous load transfer [1-3]. However, the full understanding of the failure between the adhesive and the substrate (adhesive failure) is a crucial step to surpass, in order to use adhesive bonding joints in critical systems.

For the general industry, different tests are used to measure adherence, such as the single lap joint (ISO 4 587:2003), the pull-off (ISO 6 922:1987) and, less used, the three-point bending tests (3PBT) (ISO 14679-1997) [4]. More recently, Legendre et al. [5] proposed a modified Arcan test, introducing a steel plate into the traditional Arcan sample under shear loading, resulting in an adhesive debonding. Moreover, Genty et al. (2017) [6] investigated the single lap joints, the pull-off and also the three-point bending test for the adherence measurement. Although less used, Weibull analysis showed that the 3PBT was the most reliable for interface cracking debonding. Furthermore, the 3PBT produces a located adhesive failure initiation [6-8], and for these reasons, this study selected the 3PBT test for analyzing the interface debonding.

For an identifiable initiation zone, Roche et al. (1982) [7] proposed a 3PBT relating initiation of adhesive failure to the respective load, resulting in the ISO 14679-1997 [4]. These results cannot be vastly explored, since the critical load depends on substrate thickness. For a first general approach, Sauvage et al. (2017) [8] proposed an energy-based approach, in which the dissipated energy was computed using the Euler-Bernoulli beam theory for different substrate thicknesses. Even if a located initiation zone was present, Sauvage's methodology did not consider the debonding surface. In a subsequent effort, Sauvage et al. (2019) [9] studied the influence of the stress concentration problem, evaluating the shear and peel stresses at the

crack tip. Finally, Sauvage proposed a normal stress criterion for the initiation of adhesive debonding. Nonetheless, his two approaches were not coupled with a single criterion.

Thus, using the identifiable initiation zone, this work took into account the finite fracture mechanics, by using the coupled energy and stress criterion (CC) proposed by Leguillon [10]. The assessment of the adhesive-to-adherend interface helped to overcome the previous deficiency and to consider an instantaneous and finite crack debonding. Several types of stress concentration cases applied successfully the CC, such as interface debonding by Martin et al. (2016) [11], Weißgraeber and Becker (2013) [12] and by Carrère et al. (2015) [13], on notched strength and bond strength.

Although the coupled criterion has shown to be an interesting method to study the interface cracking, most of the commercial software has implemented the cohesive zone modeling (CZM). Barenblatt (1959) [14], Dugdale (1960) [15] were the pioneers and introduced the concept, in which the singularity near to the crack tip is removed by assuming cohesive forces holding together opposite surfaces. The assessment of adhesive-to-adherend interface crack initiation via CC results in the determination of fracture toughness and critical stress. These parameters can be also exploitable by the CZM to represent interface debonding, also shown numerically by Martin et al. (2016) [11]. Thus, the CZM was applied to model the interface, bonding the substrate and the adhesive in a two-layer system.

In this work, the aim was to characterize the interface using the experimental test by the CC. The paper presents a method to assess the interface using both the macroscopic (load-displacement curve) and the mesoscopic (small round zone) measurements arising from the experimental 3PBT. Looking towards a commercial software application, the properties found by the CC were applied to predict the interface cracking by the CZM.

## **2. Experimental testing**

### 2.1. Overview of the three-point bending test

Developed by Roche (1982) [7], the test comprises an adhesive, which works as a stiffness element, bonded on a substrate. A controlled displacement was imposed on the middle of the specimen, promoting a stress concentration near to the corner between the adhesive and the substrate, resulting in an interface cracking. Figure 1 shows the dimensions of the specimens following ISO 14679-1997 [4], where  $h_s$  represents substrate thickness.

#### PBT

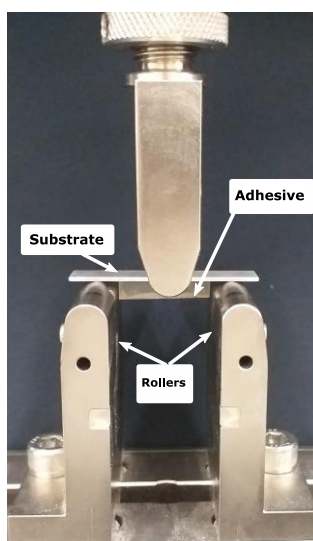


**Figure a**

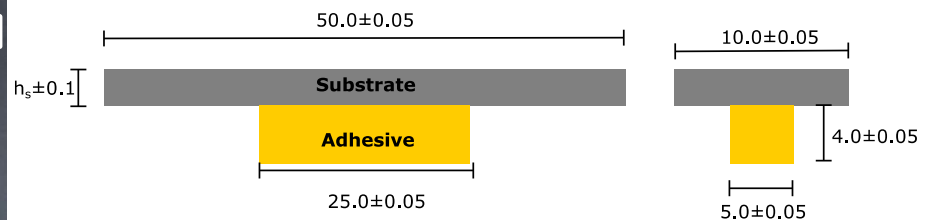


**Figure b**

**Figure 1.** (a) Three-point bending test (b) Dimensions following ISO 14679-1997 [4].

### 2.2. Material

For the three-point bending specimen preparation, the substrate was an aluminum alloy 2024-T3, supplied by Rocholl GmbH, in two different thicknesses: 1.08 mm and 1.62 mm.

The adhesive was composed of a polyepoxide bisphenol A diglycidyl ether (DGEBA) – functionality 2, supplied by Dow Chemical; a diethylenetriamine (DETA) – functionality 5 – as a hardener and the organosilane GLYMO (3-Glycidyloxypropyl)trimethoxysilane –

functionality 1, both by supplied by SIGMA-ALDRICH. The organosilane worked as an adhesion promoter and was included directly into the organic resin (5% w/w of resin).

The substrate was prepared using a simple acetone degreasing, followed by a nitric acid etching, immersing the samples in a 6.3 mol/L solution, at 50°C for 10 minutes. Finally, the samples were rinsed with de-ionized water and dried at room temperature. The acid etching formed a new and known passivation layer, removing the impurity particles, as proposed by Monteiro et al. (1988) [16]. The adhesive was produced first by mixing at room temperature the epoxy-containing substances (DGEBA and GLYMO) until a homogeneous phase was formed. Then, the DETA was introduced and mixed for 5 minutes at room temperature. The liquid was deposited into the mold, as shown in Figure 2, using a syringe, adding 0.5 ml in each space.

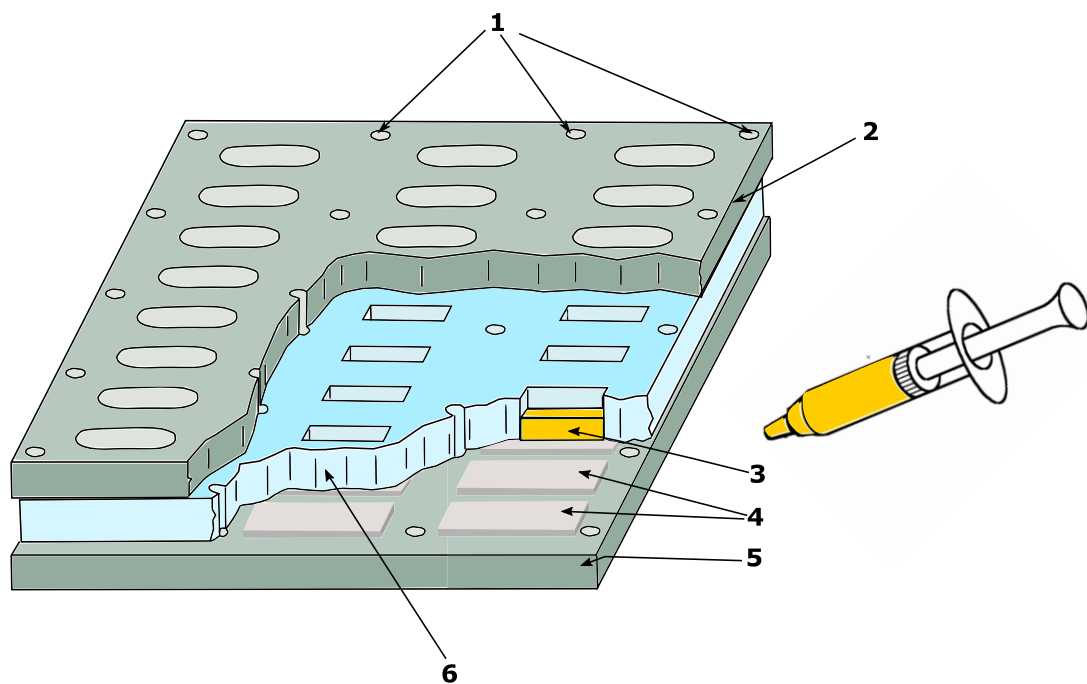


Figure 2. The conception of the samples according to ISO 14679-1997 [4] (1 – bolts, 2 – faster plate, 3 – adhesive, 4 – substrate, 5 – lower plate, 6 – silicone mold).

After the deposition, the specimens rested 4 hours at room temperature before starting the polymerization cycle. Then, the cycle comprised heating the samples until the set point temperature of 140 °C and keeping the temperature constant for 1 hour. Then, the temperature was decreased gradually to avoid residual stress. [Table 1](#) shows the properties of materials, widely known in literature and used by Sauvage et al. (2019) [9].

[Table 1](#). Mechanical properties of the materials.

	$E$ (MPa)	$\nu$
Adhesive	3000	0.35
Substrate	68000	0.33

### 2.3. Test results

For this work, the test was performed using an INSTRON tensile machine 3367, (INSTRON SA, France), adapted with a 3-point bending system with a 5 kN load sensor. Imposing a speed of 0.5 mm/min and distance of 36 mm between two rollers, the displacement is increased until a critical force, as shown in [Figure 3](#). At the critical force, an instantaneous initiation failure takes place, and the stiffness drops, showing only the substrate stiffness. The crack initiation surface can be identified in a post-mortem analysis, as shown in [Figure 3](#).

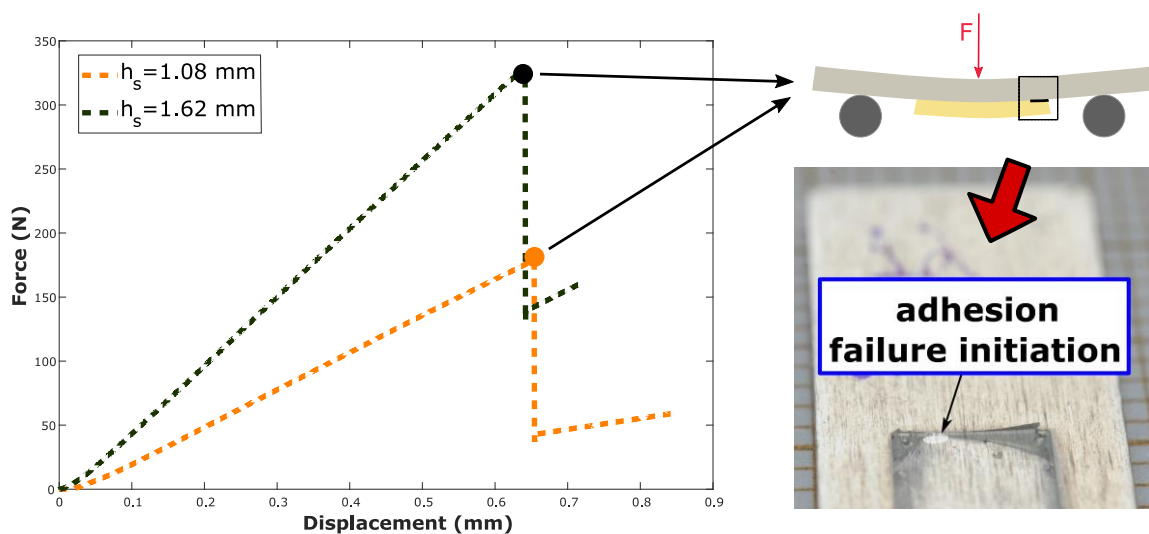


Figure 3. Three-point bending test curves and post-mortem analysis: interface cracking initiation – two different substrate thicknesses.

The small round region was then obtained by proportionality between the actual number of pixels over the small round zone and the number of pixels over a reference area taken equal to 1 mm<sup>2</sup> (millimeter paper), as shown in Figure 4.

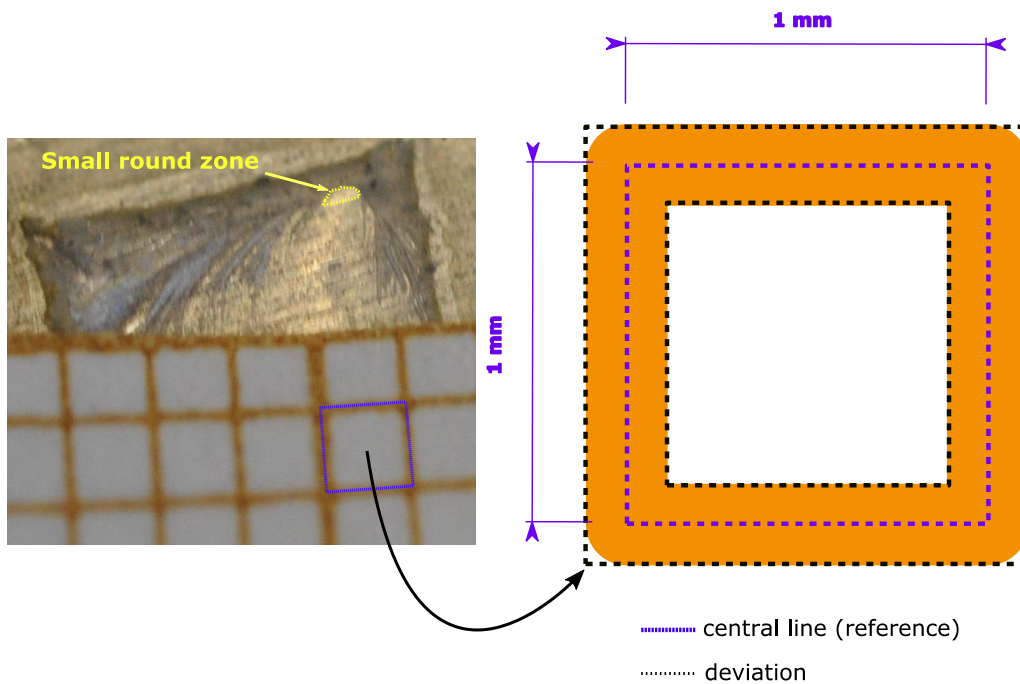


Figure 4. Reference square (1 mm<sup>2</sup>) for the surface measuring - Reference line (blue dashed line) and inner and outer line (black dashed lines).

All the standard deviations shown in Table 2 refer to the data treatment. The critical values of load  $F_c$ , displacement  $d_c$ , stiffness of specimen  $K_{spec}$  and crack surface at initiation  $S_c$  of 24 specimens were listed in Table 2. The specimen stiffness  $K_{spec}$  was determined using the least mean square, taking into account the experimental data of load and displacement in the range of  $0.2F_c$  and  $0.8F_c$  of each specimen.

**Table 2.** Results of the three-point bending test.

	$F_c$ (N)	$d_c$ (mm)	$K_{spec}$ (N/mm)	$S_c$ (mm <sup>2</sup> )
1.08 mm	$178 \pm 26$	$0.61 \pm 0.08$	$309 \pm 9$	$0.102 \pm 0.02$
1.62 mm	$326 \pm 50$	$0.64 \pm 0.09$	$535 \pm 13$	$0.07 \pm 0.01$

### 3. Analysis method

#### 3.1. 1D-beam macro-element analysis

For a fast determination of strain, stress and energy, the macro-element (ME) technique was used for modeling the specimen. The ME technique has been applied for the simplified stress analysis of hybrid joints (bonded/bolted) [17], inspired by the finite element method. The ME technique uses the local equilibrium of adherend, instead of using shape functions as traditionally performed by FE analysis. As an advantage, only one 4-nodes macro-element of length  $L_{ME}$  suffices to represent the bonded overlap  $L$  for linear elastic analysis (see Figure 5). In this section, the formulation of the ME of two bonded beams is presented firstly and briefly (see Section 3.1.1). Secondly, the model associated with the system aluminum – interface – adhesive for the 3PBT is explained in the frame of the ME technique (Section 3.1.2).

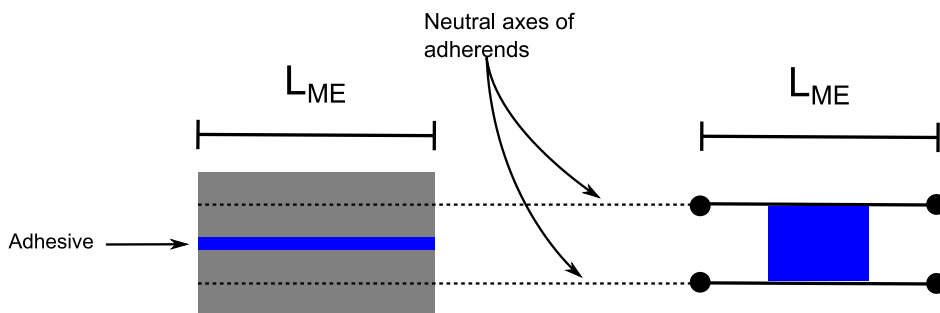


**Figure 5.** Macro-element technique representation of adhesive and adherends.

#### 3.1.1 Governing equations

Performing the global equilibrium of both adherends, considering that each node has three degrees of freedom (DOF) (see Figure 6), a system of six equations was found:

$$\begin{cases} \frac{dN_j}{dx} = (-1)^j \sigma b \\ \frac{dV_j}{dx} = (-1)^{j+1} b \tau, j = 1,2 \\ \frac{dM_j}{dx} + V_j + \frac{bh_j\tau}{2} = 0 \end{cases} \quad (1)$$

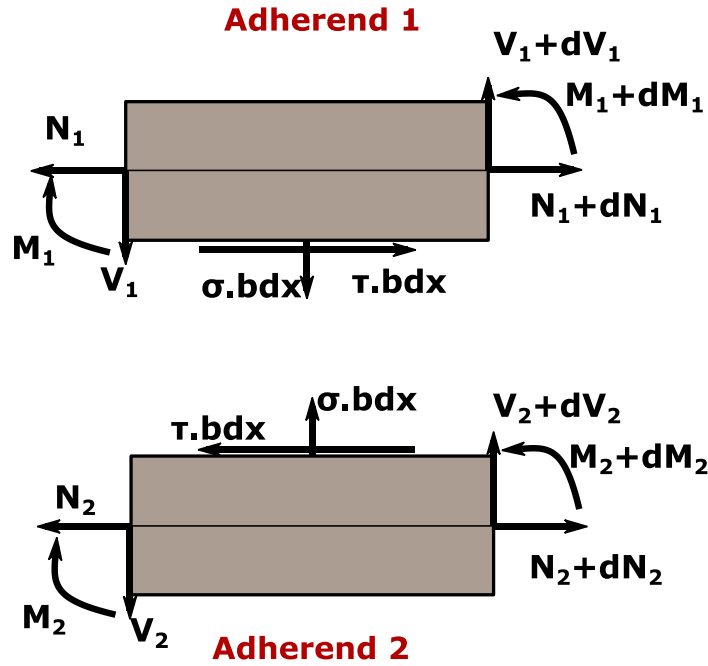


Figure 6. Internal load in an infinitesimal bonded element.

where  $N_j$ ,  $V_j$  and  $M_j$  are the normal force, shear force and bending moment, respectively, of adherend  $j$  ( $j=1$  or  $2$ ),  $b$  the overlap width,  $\sigma$  the peel stress and  $\tau$  the shear stress. Then, assuming the adherends as linear elastic Timoshenko beams, the constitutive differential equations were:

$$\begin{cases} N_j = A_j \frac{du}{dx} - B_j \frac{d\theta_j}{dx} \\ V_j = H_j \left( \frac{dw_j}{dx} - \theta_j \right) \\ M_j = -B_j \frac{du_j}{dx} + D_j \frac{d\theta_j}{dx} \end{cases} \quad j = 1,2 \quad (2)$$

where  $A_j$  is the membrane stiffness,  $D_j$  the bending stiffness,  $B_j$  the coupling stiffness,  $H_j$  the shear stiffness,  $\theta_j$  the bending angle in the adherend,  $u_j$  the displacement (mm) of adherend in the  $x$  direction and finally  $w_j$  the displacement (mm) of adherend in the  $y$ -direction, and the index  $j$  indicates the adherend. The adhesive layer was simulated as an infinite number of peel and shear springs, expressing the shear  $\tau$  and the peel  $\sigma$  stress as:

$$\tau = k_{II} \left[ u_2 - \frac{h_2 \theta_2}{2} - \left( u_1 + \frac{h_1 \theta_1}{2} \right) \right] = k_{II} \Delta u \quad (3)$$

$$\sigma = k_I [w_1 - w_2] = k_I \Delta w \quad (4)$$

where  $h_j$  is the thickness of adherend,  $k_I$  and  $k_{II}$  are the adhesive peel and shear stiffnesses, respectively. For homogeneous isotropic linear elastic adherends and with rectangular cross-sections, the stiffnesses were calculated as:

$$\begin{cases} A_j = b_j h_j E_j \\ B_j = 0 \\ D_j = \frac{b_j E_j h_j^3}{12} \\ H_j = k_{y_j} G_j b_j h_j \end{cases} \quad j = 1, 2 \quad (5)$$

where  $E_j$  is Young's modulus,  $G_j$  is the shear modulus,  $k_{y_j}$  is the shear coefficient and  $\Delta_j = A_j D_j - B_j^2 \neq 0$ . Then, substituting [Equations 3](#) and [4](#) into [1](#), a system of 12 equations was formed:

$$\left\{ \begin{array}{l}
\frac{du_1}{dx} = \frac{D_1}{\Delta} N_1 + \frac{B_1}{\Delta} M_1 \\
\frac{du_2}{dx} = \frac{D_2}{\Delta} N_1 + \frac{B_1}{\Delta} M_2 \\
\frac{dw_1}{dx} = \theta_1 + \frac{1}{H_1} V_1 \\
\frac{dw_2}{dx} = \theta_2 + \frac{1}{H_2} V_2 \\
\frac{d\theta_1}{dx} = \frac{A_1}{\Delta} M_1 + \frac{B_1}{\Delta} N_1 \\
\frac{d\theta_2}{dx} = \frac{A_2}{\Delta} M_2 + \frac{B_2}{\Delta} N_2 \\
\frac{dN_1}{dx} = -bk_{II} \left( u_2 - u_1 - \frac{h_2\theta_2}{2} - \frac{h_1\theta_1}{2} \right) \\
\frac{dN_2}{dx} = bk_{II} \left( u_2 - u_1 - \frac{h_2\theta_2}{2} - \frac{h_1\theta_1}{2} \right) \\
\frac{dV_1}{dx} = bk_I (w_1 - w_2) \\
\frac{dV_2}{dx} = -bk_I (w_1 - w_2) \\
\frac{dM_1}{dx} = -bh_1 k_{II} \left( u_2 - u_1 - \frac{h_2\theta_2}{2} - \frac{h_1\theta_1}{2} \right) - V_1 \\
\frac{dM_2}{dx} = -bh_2 k_{II} \left( u_2 - u_1 - \frac{h_2\theta_2}{2} - \frac{h_1\theta_1}{2} \right) - V_2
\end{array} \right. \quad (6)$$

To solve the system, Eq. 6 can be rewritten as  $\frac{d\mathbf{X}}{dx} = A_e \mathbf{X}$ , where  $A_e$  represents a 12x12 matrix

and  $\mathbf{X}$  the unknown vector of a macro-element, where  $\mathbf{X}^t = (u_1 \ u_2 \ w_1 \ w_2 \ \theta_1 \ \theta_2 \ N_1 \ N_2 \ V_1 \ V_2 \ M_1$

$M_2)$ . The stiffness matrix relating the nodal forces and nodal displacement was expressed as:

$$\begin{pmatrix} -N_1(0) \\ -N_2(0) \\ N_1(\Delta) \\ N_2(\Delta) \\ -V_1(0) \\ -V_2(0) \\ V_1(\Delta) \\ V_2(\Delta) \\ -M_1(0) \\ -M_2(0) \\ M_1(\Delta) \\ M_2(\Delta) \end{pmatrix} = K_e \begin{pmatrix} u_1(0) \\ u_2(0) \\ u_1(\Delta) \\ u_2(\Delta) \\ w_1(0) \\ w_2(0) \\ w_1(\Delta) \\ w_2(\Delta) \\ \theta_1(0) \\ \theta_2(0) \\ \theta_1(\Delta) \\ \theta_2(\Delta) \end{pmatrix} \quad (7)$$

The determination of the fundamental matrix of  $A_e$ , named  $\Phi_A$ , is an essential step to calculate

$K_e$ .  $\Phi_A$  is calculated at  $x=0$  and  $x=L_{ME}$ , as indicated in Figure 7 using the exponential matrix:

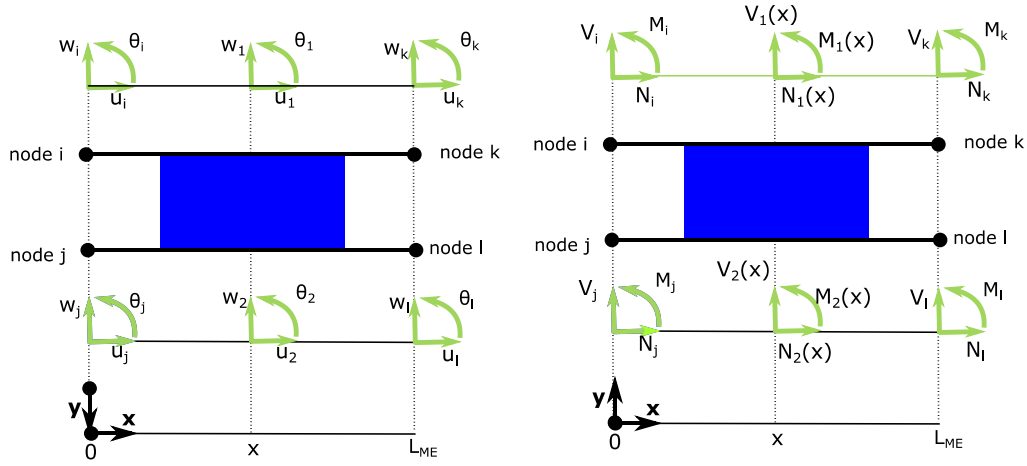


Figure 7. Bonded beam element of four-nodes macro element: nodal displacement and force in the adherends.

$$\begin{cases} \Phi_A(x=0) = \expm(A_e \cdot 0) \\ \Phi_A(x=\Delta) = \expm(A_e \cdot \Delta) \end{cases} \quad j = 1,2 \quad (8)$$

From the equations, two different matrices were obtained (size 12x12)  $M_e'$  and  $N_e'$ : the first matrix represents the lines related to the nodal displacement, whereas the second was related to nodal forces. For both matrices, the first six lines correspond to the position at  $x=0$  and the last six correspond to the position at  $x=\Delta$ .

$$\begin{cases} M_e' = \Phi_u(0, \Delta) = \begin{pmatrix} [\Phi_A(x=0)]_{i=1:6; j=1:12} \\ [\Phi_A(x=\Delta)]_{i=1:6; j=1:12} \end{pmatrix} \\ N_e' = \Phi_f(0, \Delta) = \begin{pmatrix} [\Phi_A(x=0)]_{i=7:12; j=1:12} \\ [\Phi_A(x=\Delta)]_{i=7:12; j=1:12} \end{pmatrix} \end{cases} \quad (9)$$

As shown in Equation 7, the stiffness matrices must be arranged according  $K_e$ , in this case  $(u_1(0) \ u_2(0) \ u_1(\Delta) \ u_2(\Delta) \ w_1(0) \ w_2(0) \ w_1(\Delta) \ w_2(\Delta) \ w_1(0) \ w_2(0) \ w_1(\Delta) \ w_2(\Delta))$  and then, the coupling matrix  $M_e$  was produced. In the same way, the coupling matrix  $N_e$  was arranged following the same operation and multiplying by -1 the terms related to the nodal forces at  $x=0$   $(-N_1(0) \ -N_2(0) \ N_1(\Delta) \ N_2(\Delta) \ -V_1(0) \ -V_2(0) \ V_1(\Delta) \ V_2(\Delta) \ M_1(0) \ M_2(0) \ M_1(\Delta) \ M_2(\Delta))$ . After establishing both matrices [17], the stiffness matrix was calculated such as:

$$K_e = N_e \cdot M_e^{-1} \quad (10)$$

Thus, once the matrix stiffness was calculated, the global assembly of matrix and all the loads and displacement could be determined.

3.1.2. Modeling of 3PBT with the ME technique

For the modeling of the 3PBT using the ME technique, the aluminum plate, the adhesive bulk and the adhesive/substrate interface were represented as adherend 1, adherend 2 and a bed of peel and shear springs, respectively (see Figure 8). Using the symmetry according to the y-axis, a displacement was imposed in the middle of the specimen. For the symmetrical adherend/interface/adhesive model, the y-displacement was fixed on the left side, while the x-displacement and the rotation in the middle of the specimen were also fixed. In addition, the total length of the bonded overlap was  $L=25\text{ mm}$ .

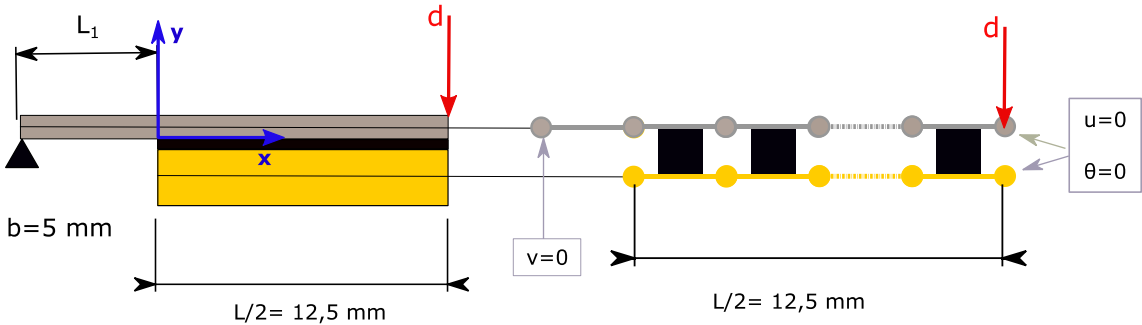


Figure 8. Three-point bending specimen – Macro-element representation.

For a linear elastic analysis, the mesh density did not affect the convergence. However, for non-linear analysis, the mesh density influenced the value of the critical force, as shown further. In addition, for the real case, two cylinders were in contact with the aluminum substrate, and thus, different from the modeled boundary condition. For that reason, the length outside the overlap  $L_l$  must be adapted to match both the experimental and the numerical stiffnesses.

### 3.2. Coupled energy and stress criterion

Based on the finite fracture mechanics, Leguillon (2002) [10] proposed a coupled energy and stress criterion to predict the critical load and the instantaneous finite crack length when a high-stress level is present. Two conditions are necessary to be fulfilled simultaneously for crack initiation. Based on the Griffith criterion, in the case of sufficiently brittle materials, for infinitesimal crack growth and neglecting the kinetic energy, the total energy release rate is equivalent to fracture toughness  $\mathcal{G}_c$ :

$$\mathcal{G} = -\frac{\partial W}{\partial S} \geq \mathcal{G}_c \quad (11)$$

where  $W$  represents the potential energy and  $S$  the crack surface. However, considering the finite fracture mechanic analysis, the assumption of the infinitesimal crack length is not valid: in this case, a finite crack surface was used and by consequence, an incremental energy release rate was used:

$$\mathcal{G}_{inc} = -\frac{\Delta W}{\Delta S} \geq \mathcal{G}_0 \quad (12)$$

The Equation 12 represented the first condition necessary. In addition, the differential and the incremental energy release rate were related by:

$$\mathcal{G}_{inc} = \frac{1}{\Delta S} \int_S^{S+\Delta S} \mathcal{G}(\Omega) d\Omega \quad (13)$$

For a 2D analysis, the crack surface was defined by  $\Delta S=ba$ , where  $a$  is the crack length. Thus, assuming the crack surface defined in the whole bonded width, the incremental energy release rate was determined as:

$$\mathcal{G}_{inc} = \frac{1}{a} \int_0^a \mathcal{G}(x) dx \quad (14)$$

Even though possible, the determination of incremental energy release rate as a function of mode mix is hard to obtain, requiring empirical relations (Banks-Sills). Using the same approach as Martin et al. (2016) [11], the mode mix was not considered by the assumption

$$\sigma_c = \tau_c.$$

The second condition necessary for the coupled criterion (CC), required that the whole surface has exceeded the tensile stress, referred as point stress criterion:

$$\sigma_{eq}(\mathbf{x}) \geq \sigma_c \forall \mathbf{x} \in S \quad (15)$$

When the energy release rate has a monotonic increase whereas the equivalent stress has a monotonic decrease, the inequalities (12) and (15) are transformed into equalities, providing a lower ( $a_{min}$ ) and an upper ( $a_{max}$ ) bound of the crack length, respectively. Thus, the problem can be converted into an optimization problem, which means the searching of the lowest load satisfying both criteria ( $a_{min} = a_{max}$ ).

As proposed by Cornetti et al. (2012) [18], the interface was modeled as a bed of peel and shear springs, such as presented in Section 3.1 with the interface stiffnesses  $k_I$  and  $k_{II}$ .

First of all, for the equivalent stress determination, the stress condition used near the crack tip was the same proposed by Martin et al. (2016) [11]:

$$\sigma_{eq}(x, y = 0) = \sqrt{\left(\frac{\sigma(x, y=0)}{\sigma_c}\right)^2 + \left(\frac{\tau(x, y=0)}{\tau_c}\right)^2} \geq 1 \forall x \leq a \quad (16)$$

where  $a$  is the crack length and the coordinates were shown in Figure 8.

At first, the mode mix was not considered, by assuming  $\sigma_c = \tau_c$ . Thus, the equivalent stress was expressed as:

$$\sigma_{eq}(x) = \sqrt{\sigma^2(x) + \tau^2(x)} \geq \sigma_c \forall x \leq a \quad (17)$$

For the CC cases listed in Section 1, given the properties of the material, the goal was to find the lowest load that satisfied both conditions (Eq. 12 and 17) and thus determining  $F_c$  and  $a_c$ . However, in this work, the former variables were already available from the post-mortem analysis ( $a_c$ ) and the load sensor of the INSTRON machine. Hence, the determination of the properties did not require an optimization algorithm, only the direct application of Eq. 12 and 16 to determine the critical stress and critical energy release rate, as will be explained further.

### 3.3. Energy release rate and fracture length model

A crucial part for the coupled criterion is the determination of the energy release rate, which is estimated using the J-integral, taking into account directly the mode I and mode II energies:

$$J = \int W dy - \mathbf{T} \frac{\partial \mathbf{u}}{\partial x} ds, \quad \mathbf{T} = \boldsymbol{\sigma} \cdot \mathbf{n} \quad (18)$$

where  $W$  is the strain energy density,  $\mathbf{T}$  the traction vector,  $\mathbf{u}$  the displacement vector,  $s$  the curvilinear abscissa,  $\boldsymbol{\sigma}$  the stress tensor and  $\mathbf{n}$  the vector normal to the path. Fraise and Schmit (1993) [19] proposed the J-integral formulated in terms of internal loads, based on the Timoshenko's Beam approach for the closed path ABCDEFGHA (see Figure 9):

$$J = \frac{1}{2b} \left[ \frac{1}{A_1} (N_1^2 - N_1'^2) + \frac{1}{D_1} (M_1^2 - M_1'^2) + \frac{1}{H_1} (V_1^2 - V_1'^2) \right] + \frac{1}{2b} \left[ \frac{1}{A_2} (N_2^2 - N_2'^2) + \frac{1}{D_1} (M_2^2 - M_2'^2) + \frac{1}{H_1} (V_2^2 - V_2'^2) \right] + 1/b [V_1' \theta_1' - V_1 \theta_1 + V_2' \theta_2' - V_2 \theta_2] \quad (19)$$

where  $N_j$ ,  $V_j$  and  $M_j$  are determined at  $a_c/2$  (crack tip), while  $N'_j$ ,  $V'_j$  and  $M'_j$  are determined at  $d_{far}=0.4L$  from the corner of adhesive and substrate, as shown in Figure 9.

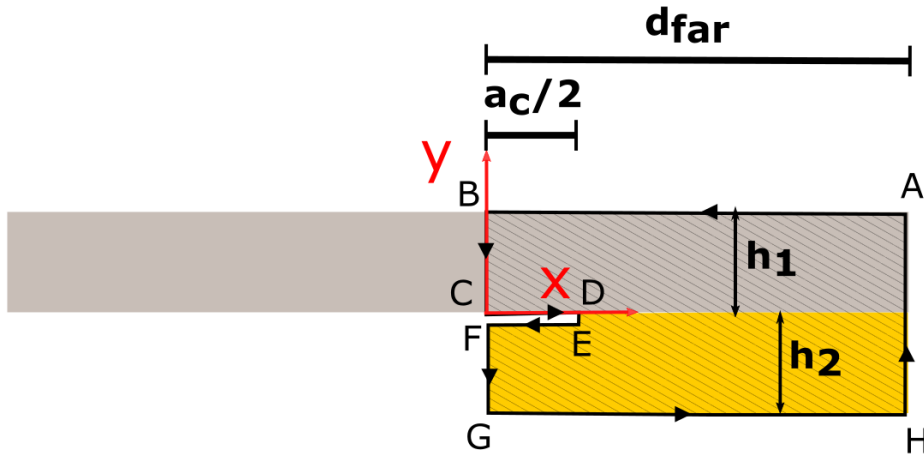


Figure 9. J-integral path and points for calculation of internal load –  $a_c/2$  and  $d_{far}$ .

However, despite the J-integral being a suitable solution for determining the critical energy release rate, Eq. 19 is only valid for substrates with the same width  $b$ . As shown before, the three-point bending specimen had a different width for the bulk polymer ( $b_a$ ) and for the

metallic substrate ( $b_s$ ). Thus, an equivalent specimen must be used, as shown in Figure 10. The new equivalent Young's modulus, conserving the global stiffness of the substrate, is expressed as:

$$E_s^* = \frac{b_s}{b_a} E_s \quad (20)$$

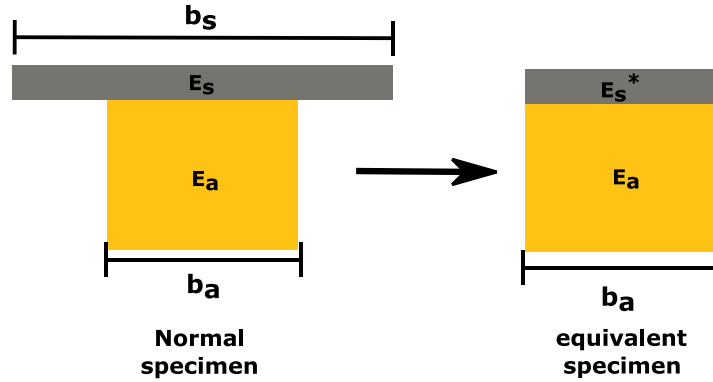


Figure 10. The equivalent cross-section for energy release rate determination, using the reference width as  $b=b_a$ .

The last step to determine  $\mathcal{G}_{inc}$  was the definition of an equivalent crack length  $a_c$ . As demonstrated before, a small round zone appears near the tip of the overlap when the critical force is reached. Thus, for creating a 1D crack, the assumption was a narrow crack strip over the whole width, as shown in Figure 11. Hence, the equivalent  $a_c$  was calculated as:

$$\frac{a_c}{2} = \frac{S_c}{b_a} \quad (21)$$

Once  $\mathcal{G}$  was computed, the  $\mathcal{G}_{inc}$  could be calculated using the Eq. 14.

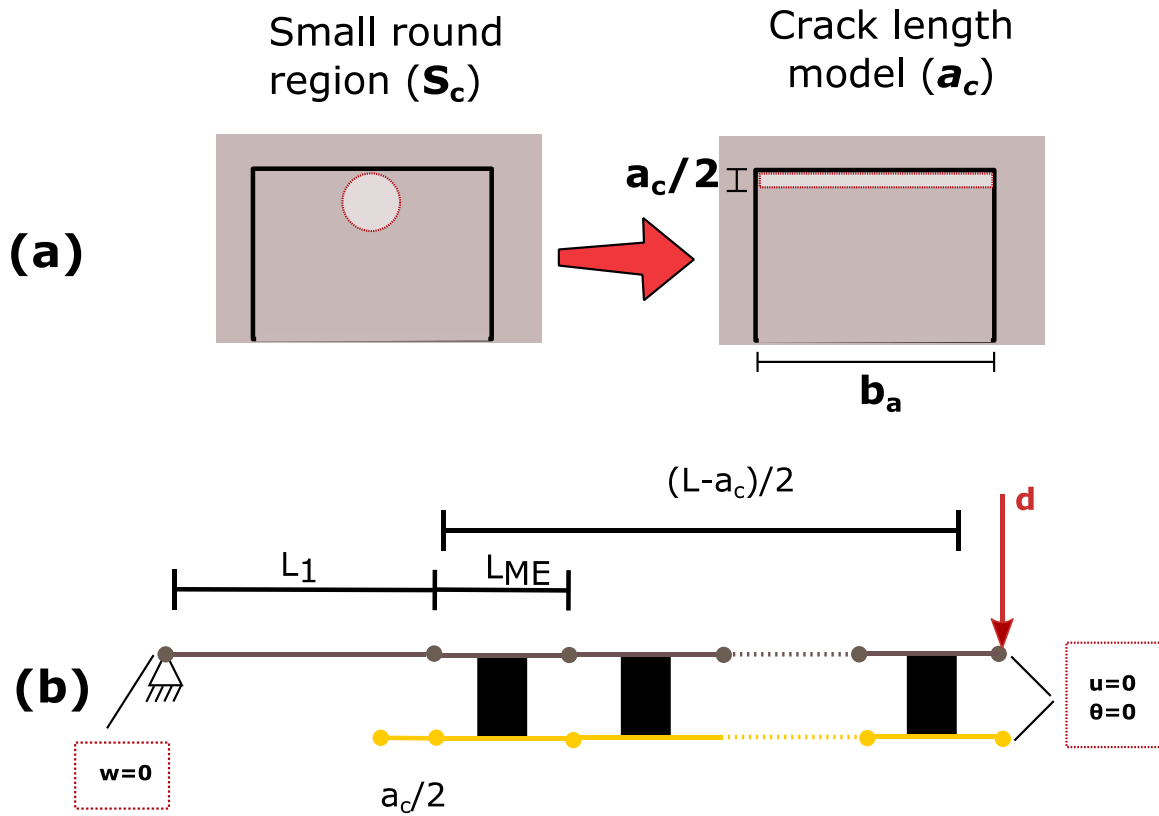


Figure 11. (a) Equivalent fracture length for the energy release rate determination. (b) Macro-element model for the energy release determination.

#### 4. Assessment of interface properties

Before starting the analysis, the first step was adjusting the outer length  $L_1$  to match the ME model with the experimental test, because of the different boundary condition. Then, using the experimental specimen stiffness, the interface adjustment stiffness was computed, fitting the global response of the numerical simulation with the experimental stiffness (2<sup>nd</sup> step), as shown in Figure 12.

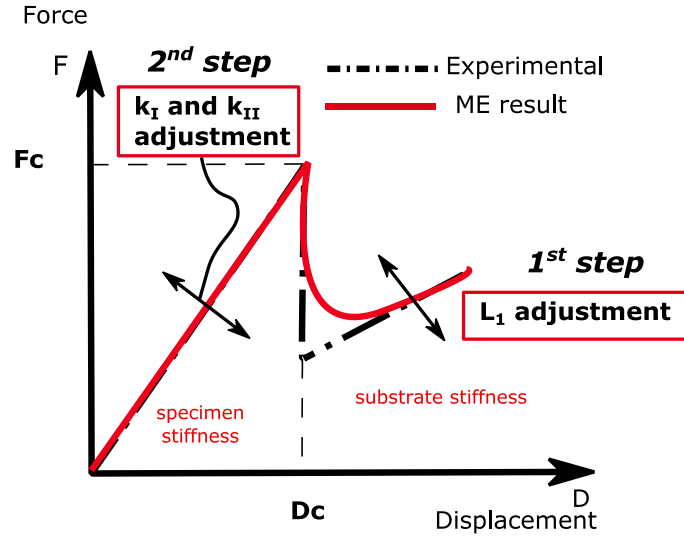


Figure 12. Adjustment of  $L_1$  and adjustment stiffnesses for comparing experimental and numerical results.

The experimental specimen stiffness does not depend on the surface treatment, and consequently neither the interface adjustment stiffness. The adjustment stiffness depends only on the global response of the specimen and not on the interaction between the adhesive and the substrate. The aim of these steps was to provide a simplified model that was as most representative as possible of the real boundary conditions. The free length  $L_1$  was then adjusted using the least mean square method. Then,  $L_1$  was found equal to 5.45 mm for  $h_s=1.08$  mm and  $L_1=5.42$  mm for  $h_s=1.62$  mm. These adjusted lengths were very close to the real value and included in the tolerance fitting. Hence, the adjusted value was assigned to the actual value  $L_1=5.5$  mm. For the interface adjustment stiffness, there were infinite combinations of  $k_I$  and  $k_{II}$  to fit the numerical with the experimental stiffness, as shown in Figure 13. The shear stiffness can be expressed as a function of peel stiffness  $k_{II}=\alpha k_I$  multiplying by a factor  $\alpha$ , defined as a shear/peel stiffness ratio.

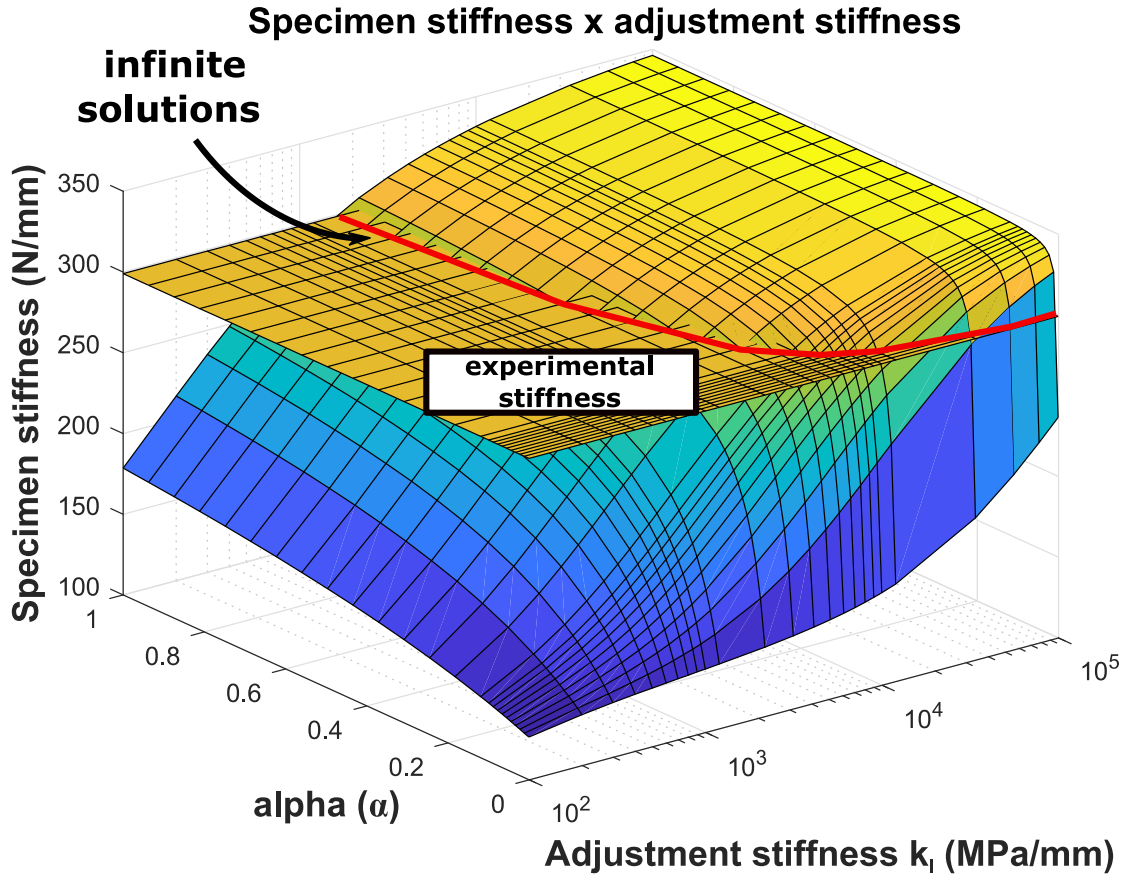


Figure 13. Adjustment of  $L_I$  and the adjustment stiffness  $k_I$  for comparing experimental and numerical results –  $h_s=1.08$  mm.

However, the pre-state condition, by the assumption of no differentiation between mode I and II supposing  $k_I=k_{II}$ , resulted in a single solution. Performing a sensibility analysis, the  $\mathcal{G}_{inc}$  (Eq. 19 and Eq. 14) and the  $\sigma_c$  (Eq. 17) were determined for different  $k_I$  and  $k_{II}$  using CC. As result,  $\sigma_c$  (Figure 14-a) increased for high values of stiffness, whereas  $\mathcal{G}_{inc}$  had an asymptotical behavior, as demonstrated in Figure 14-b.

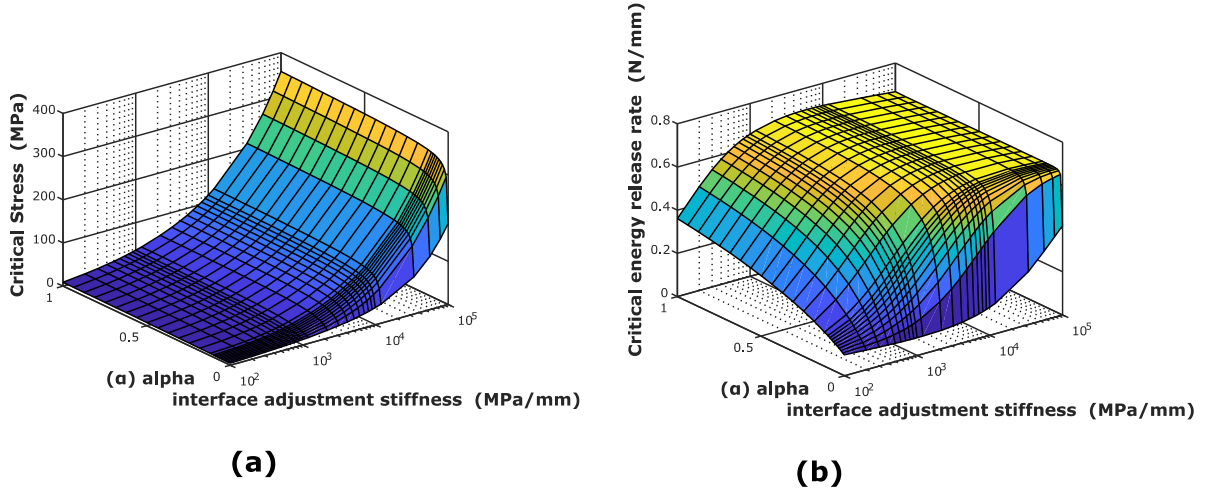


Figure 14. (a) Critical stress and (b) critical energy release rate in function of adjustment stiffness.  $h_s=1.08 \text{ mm}$ .

Using a simple linear elastic analysis with the macro-element technique, imposing  $k_I=k_{II}$  and  $L_I=5.5 \text{ mm}$ , the adjustment stiffness was  $2000 \text{ MPa/mm}$  for  $h_s=1.08 \text{ mm}$ . Hence, the coupled criterion was applied to compute the fracture parameters of the interface. Carrère et al. (2015) [13] highlight that, from the physical point of view, the stress criterion in the CC ensures the creation of micro-cracks, while the energy criterion is responsible for the propagation of micro-cracks up to a macroscopic crack. In this paper, the small round zone was assumed to be this macro-crack, formed at the peak load.

Finally, Table 3 showed the results from the coupled criterion for the  $h_s=1.08 \text{ mm}$ .

Table 3. Properties of interface determined using the coupled criterion.

$h_s \text{ (mm)}$	$\mathcal{G}_c \text{ (N/mm)}$	$k_I = k_{II} \text{ (MPa/mm)}$	$\sigma_c \text{ (MPa)}$
1.08	0.687	2000	52.4

The precision of surface evaluation and its influence were also important facts to estimate the fracture parameters. For minimizing the line width effect of the millimeter paper, the reference square was taken as a line passing through the half-width of the orange square, as shown in Figure 4 in Section 2.3.

The maximum measuring/optical error considering the maximum and the minimal square was evaluated as  $\pm 22\%$  concerning the central line. Then, the CC algorithm was tested considering the surface deviation, thus  $1.22S_c$  and  $0.78S_c$ . As shown in Figure 15, the influence of the error on  $\sigma_c$  was 0.4%, while on  $G_{inc}$  was negligible.

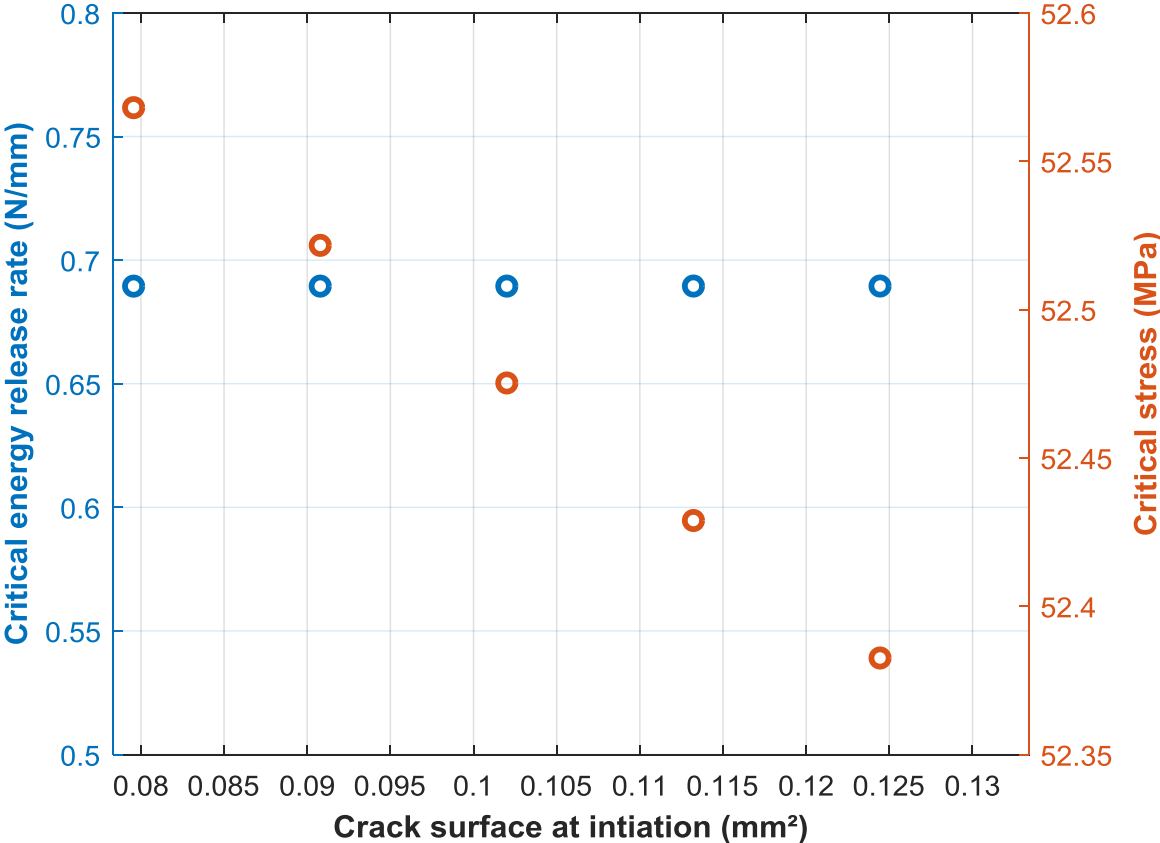


Figure 15. Influence of the surface measuring error on the interfacial properties.

5. Cohesive zone modeling application

Well-known in commercial software, the cohesive zone modeling has been an interesting tool to predict the interface cracking, for both initiation and propagation. However, up-to-now, the determination of interface parameters is hard to establish, requiring experimental analysis. In this work, the idea was to analyze the global behavior of a bonded joint using the CZM, in which the damage evolution was described by the properties identified by the CC.

In this method, the evolutions of the stresses were described in function of the displacement across the faces along the process zone. Many propositions of two-dimensional behavior curves can be used to describe the damage along the process zone.

For this paper, a bilinear function [20] described by the parameters found via CC, was used (see Figure 16). The CZM was applied for the ME technique, using a Newton-Raphson algorithm to determine the secant stiffness and updating at each iteration. The classical displacement-based method was employed to assess the damage parameter in a simple manner. It is remembered that the aim of this study was not to introduce a methodology to determine a cohesive zone model from the analysis of the 3PBT. The idea developed in this last section was to test the use of simplified CZM (displacement-based, no mode differentiation), the parameters of which come from CC-based methodology associated with the 3PBT, to simulate the 3PBT. The adhesive was assumed to have a classical bilinear damage evolution, involving interaction energy laws for both initiation and propagation under mixed-mode:

$$\begin{cases} \left(\frac{G_I}{G_{Ie}}\right)^n + \left(\frac{G_{II}}{G_{IIe}}\right)^n = 1 \\ \left(\frac{G_I}{G_{Ic}}\right)^m + \left(\frac{G_{II}}{G_{IIc}}\right)^m = 1 \end{cases} \quad (22)$$

where  $n=m=1$ ,  $G_{Ic}$  and  $G_{IIc}$  are the critical strain energy release rate in mode I and mode II,  $G_{Ie}$  and  $G_{IIe}$  are the elastic strain energies stored in mode I and mode II and  $G_I$  and  $G_{II}$  are related to the strain energy release rates in mode I and mode II, respectively.

The norm of displacement jump (in mm) of the interface  $\lambda$  was defined by:

$$\lambda = \sqrt{(\delta_v)^2 + (\delta_u)^2} \quad (23)$$

where  $\delta_v$ , ( $\delta_u$ ) is the displacement jump of the interface along the y-axis (x-axis). A mixity parameter  $\beta$  was defined by:

$$\beta = \frac{\delta_u}{\delta_v} = \frac{u_2 - u_1 - h_2 \theta_2 - h_1 \theta_1}{v_1 - v_2} \quad (24)$$

At each iteration, the mixity parameter  $\beta$  was updated. Under the current local mixity parameter, a bilinear law was assumed for the material, so that the damage parameter  $D$  was such that:

$$D = \frac{\lambda_f(\lambda - \lambda_e)}{\lambda(\lambda_f - \lambda_e)} \quad (25)$$

where  $\lambda_e$  ( $\lambda_f$ ) is the displacement jump (in mm) of the interface at initiation (propagation). In order to compute  $\lambda_e$  ( $\lambda_f$ ), the interaction laws Eq. (22) were used while classically assuming that the projections on pure modes of the mixed-mode evolution law under the current local mixity were bilinear:

$$\begin{cases} \lambda_e = \delta_{ue} \delta_{ve} \sqrt{1 + \beta^2} \left[ \frac{1}{(\delta_{ue})^{2n} + (\beta \delta_{ve})^{2n}} \right]^{\frac{1}{2n}} \\ \lambda_f = \delta_{uf} \delta_{vf} \sqrt{1 + \beta^2} \left[ \frac{\sqrt{(\delta_{ue})^{2n} + (\beta \delta_{ve})^{2n}}}{(\delta_{ue} \delta_{uf})^n + (\beta^2 \delta_{ve} \delta_{vf})^n} \right]^{\frac{1}{n}} \end{cases} \quad (26)$$

The damage parameter was computed only if  $\delta_v$  was positive. In this paper, no mode I and mode II differentiation was assumed. As a result, the expressions provided in Equation. 26 become:

$$\begin{cases} \lambda_e = \delta_{ue} = \delta_{ve} \\ \lambda_f = \delta_{uf} = \delta_{vf} \end{cases} \quad (27)$$

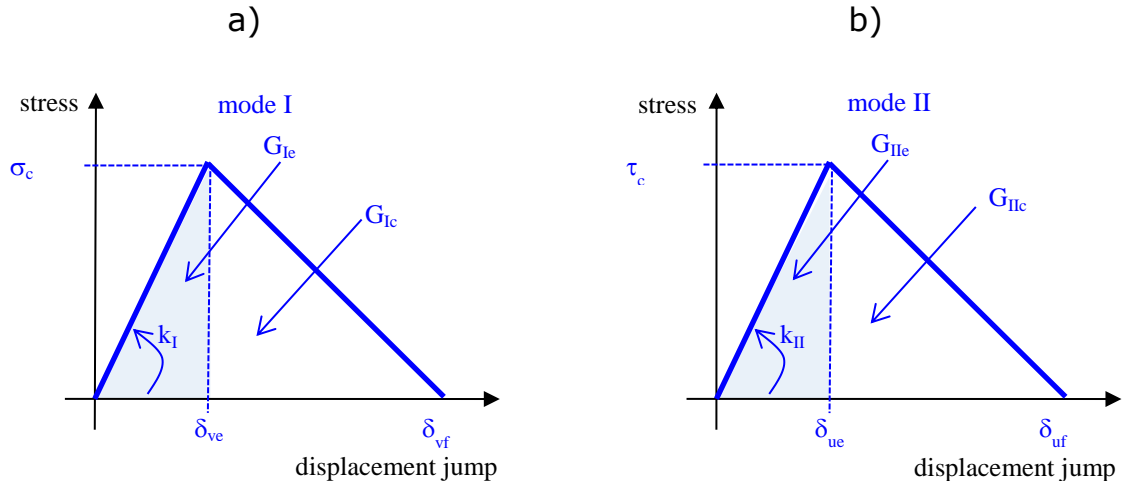


Figure 16. Bilinear behavior function. a) In pure mode I. b) in pure mode II.

A unique damage parameter  $D$  was required for each ME. It was chosen equal to the maximal value of damage parameters computed at each of both pairs of nodes was assigned to each ME. Moreover, if the damage parameter computed was strictly higher than a prescribed value, then  $D$  was fixed to this value, which was chosen equal to 0.9999999 in this paper.

The softening law shown in the Figure 16 had three phases: (I) the increase of stress until a critical value, corresponding to an undamaged part; (II) the stress uncharged region and loss of the stiffness after the critical stress, corresponding the development of damaged region; and finally (III) the creation of a stress-free surface, after reaching the critical displacement jump.

The fracture energy, which controls the damage propagation, was calculated as:

$$G_{Ic} = G_{IIc} = G_c = \frac{\sigma_c \lambda_f}{2} \quad (28)$$

Because most of the finite element based software implemented the cohesive zone modeling, this section explored the properties determined via CC as input for the behavior law of damage of interface.

An important fact noticed by Martin et al. (2016) [11] was that the CC and the CZM were in good agreement for low “fracture length” defined in terms of the material properties and interface thickness  $e_a$ , such as:

$$\left(\frac{L_c}{e_a}\right)^* = \frac{k_I G_c}{\sigma_c^2} \quad (29)$$

Assuming the unit value for the interface thickness, the fracture length represents a method to evaluate if a material is ductile or brittle, similar to the brittleness number described by Weißgraeber and Becker (2013) [12]. For a brittle behavior, the fracture toughness can be determined in terms of the critical stress and the adjustment stiffness, such as  $G_c = \sigma_c^2 / (2k_I)$ , resulting in a fracture length  $L_c^* = 0.5$ . In this paper, the fracture length of the interface was  $L_c^* = 0.501$ , indicating a quasi-brittle behavior. For evaluating the capacity of the coupled criterion to predict the damage behavior of the CZM, the same parameters shown in Table 3 were tested in the bilinear behavior law. From now, since a non-linear behavior was present, a mesh convergence test was required, testing five different mesh densities; however, only three were shown in Figure 17. A negligible variation of the critical load was found between the lower and the higher mesh density.

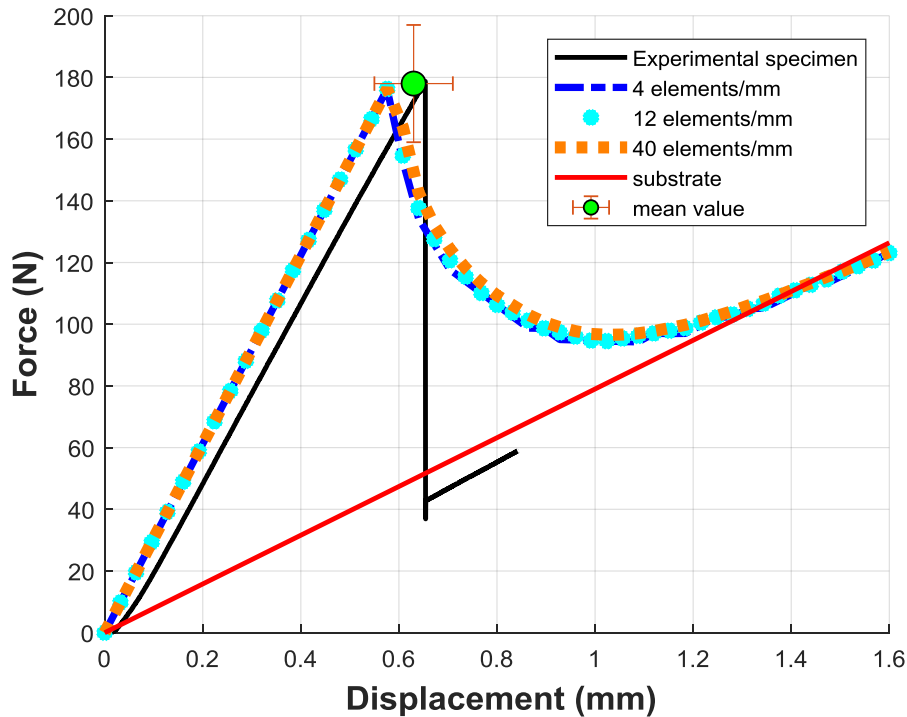


Figure 17. Mesh convergence test -  $h_s = 1.08 \text{ mm}$

Moreover, the evaluation of the crack length at initiation was an important factor to observe. The crack growth and its convergence for different mesh densities were shown in Figure 18, indicating a good agreement between different values computed.

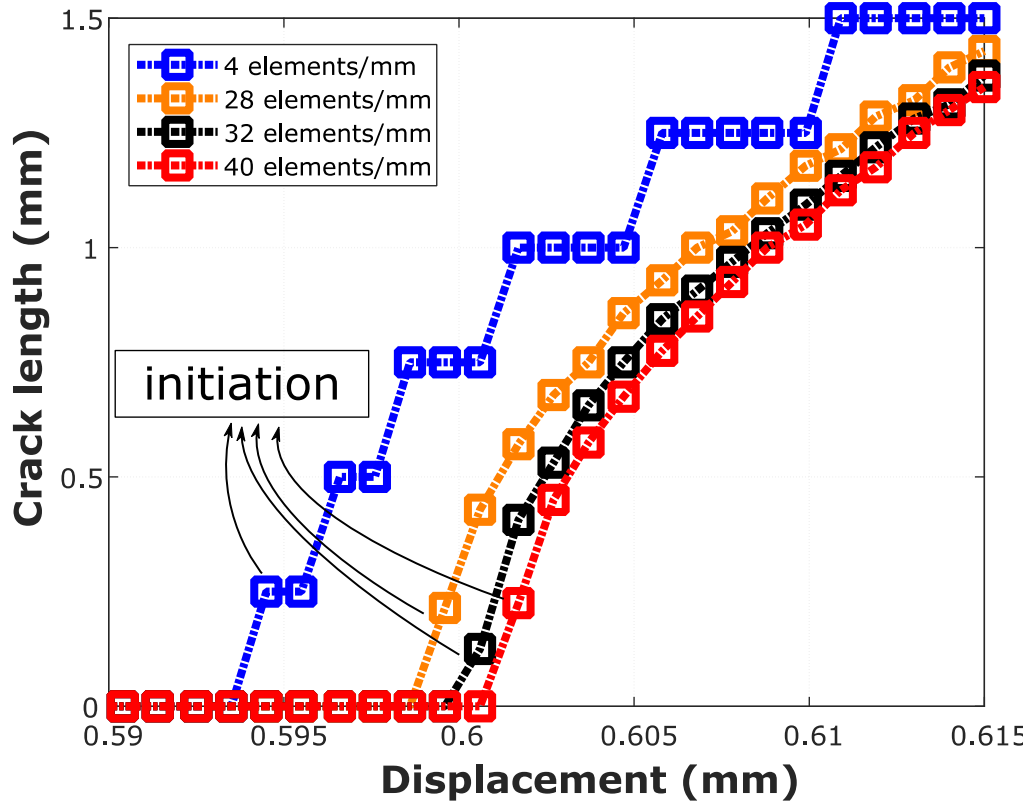


Figure 18. Interface cracking convergence for different mesh densities according to the initiation criterion -  $h_s=1.08$  mm.

On the other hand, for a real representation of the crack length, a high mesh density was required. For this purpose, a refinement zone was created in the first 0.5 mm of the overlap and only one macro-element for the remaining zone. Moreover, the whole refinement zone should be ensured in the process zone, as shown on the left of Figure 19, on the right corner. In other words, the number of damaged elements must be less than the number of elements of the process zone ( $n_{proc} < n_{ref}$ ). Using this refinement, each element in this zone had a length of  $L_{ref}=0.8$   $\mu m$ . Then, after the critical force, the numbers of completely damaged elements  $n_{dam}$  were counted, indicating the crack length in an indirect way.

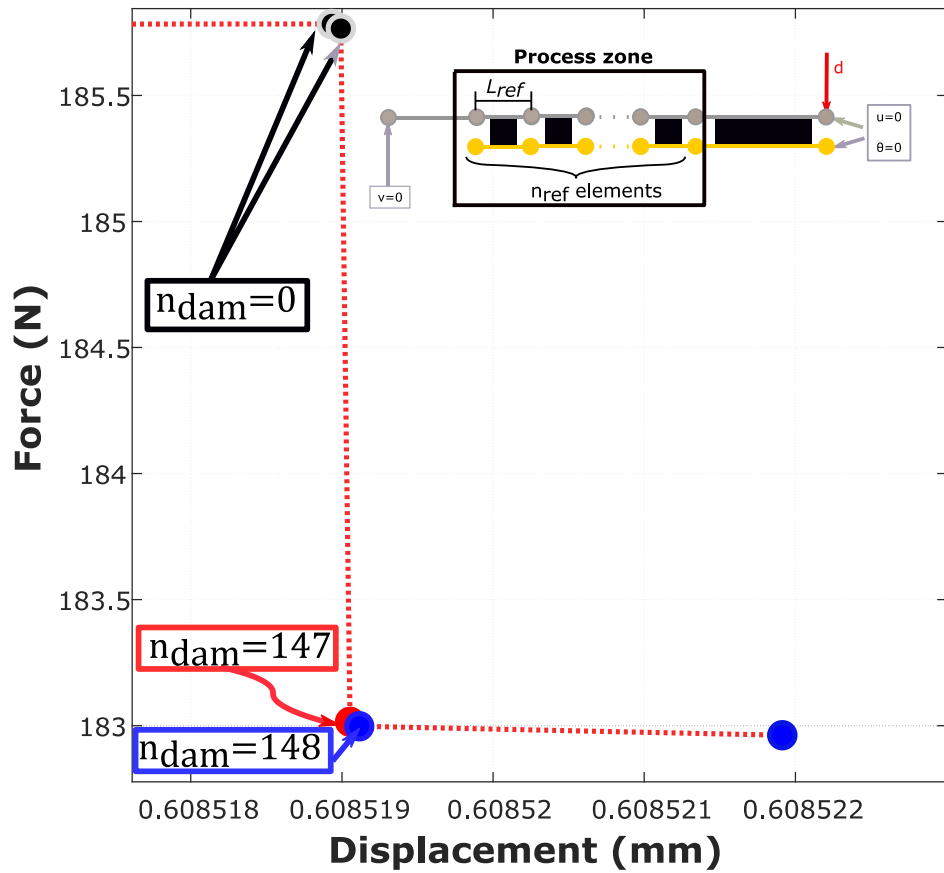


Figure 19. Zoom in the load x displacement curve (Figure 18) at the initiation of interface cracking using the refinement of  $L_{ref}=0.8 \mu m$ .

As shown in Figure 19, immediately after the critical force, the numerical solution had a quasi-instantaneous load drop of 2.82 N and then, a stable propagation (blue points in Figure 19). The crack size at initiation determined by the CZM was  $a_{czm}/2=0.118 \text{ mm}$ , greater than the result found experimentally. Therefore, the crack length calculated by the refinement method was in accordance with those values using different regular mesh densities. This fact indicated a limitation of the choice of the method for the computation of the damage parameter to represent the effects in a mesoscale (crack initiation), even if the macroscale (critical displacement and critical force) was accurate. A restricted influence study of the crack length used as an input on the critical stress and the critical energy release rate was

undertaken. As shown in [Figure 15](#), the  $\mathcal{G}_c$  was significantly less affected than the critical stress. Moreover, for a crack length 5 times higher than the measured crack length, the deduced critical stress decreased from 3.2%. This difference did not appear significant on the global mechanical response. The influence of the critical stress was then probably restricted when the critical energy release rate remained almost constant. In other words, the assessment of  $\sigma_c$  could be more difficult than the  $\mathcal{G}_c$  thanks to the analysis of the experimental tests through the present methodology. A detailed sensitivity analysis including the uncertainty of experimental data should be performed to assess the robustness of the present method.

The fracture parameters of the interface were only affected by the surface preparation, polymerization cycle and by the room conditions. Hence, the fracture parameters of the interface found previously must be able to predict the adhesive debonding for  $h_s=1.62 \text{ mm}$ . Using the properties of the interface found before, a mesh study was performed again for the thicker substrate. The critical values for displacement and force were in good agreement with the experimental test, as shown in [Figure 20](#).

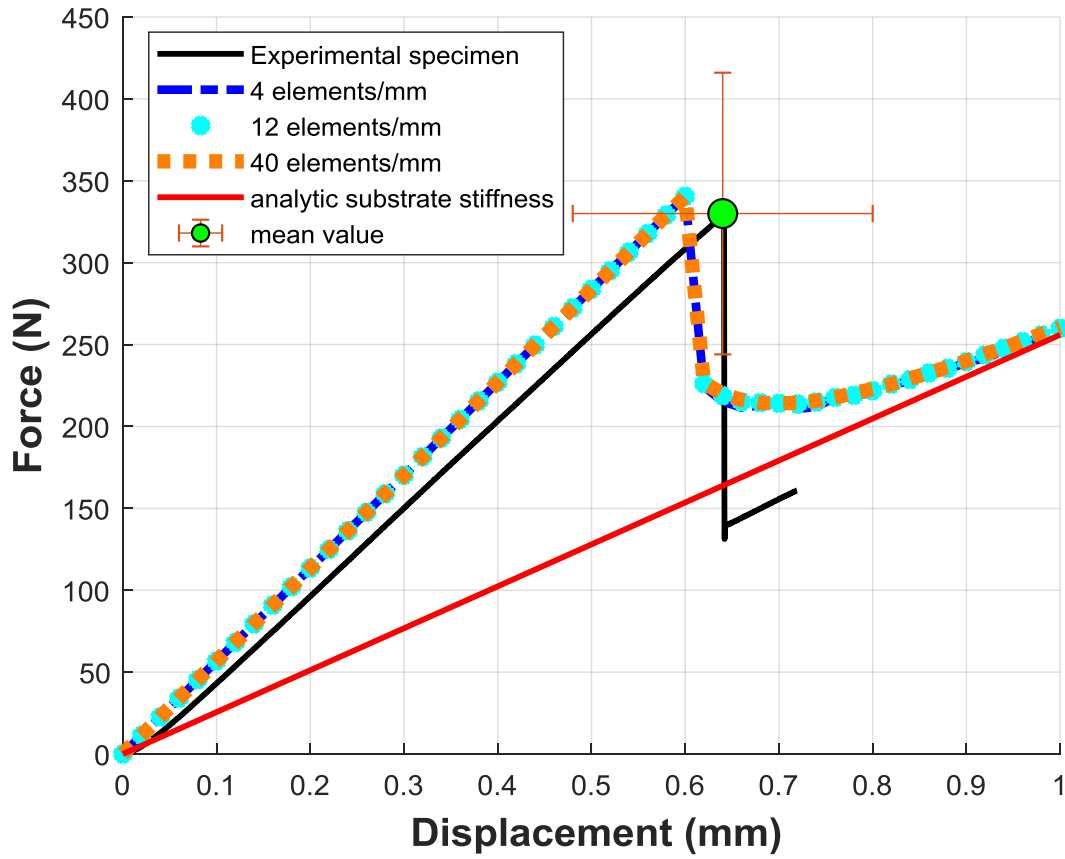


Figure 20. Mesh convergence test -  $h_s=1.62$  mm.

The crack growth for different mesh densities was performed, and again, a numerical convergence was found, as shown in Figure 21.

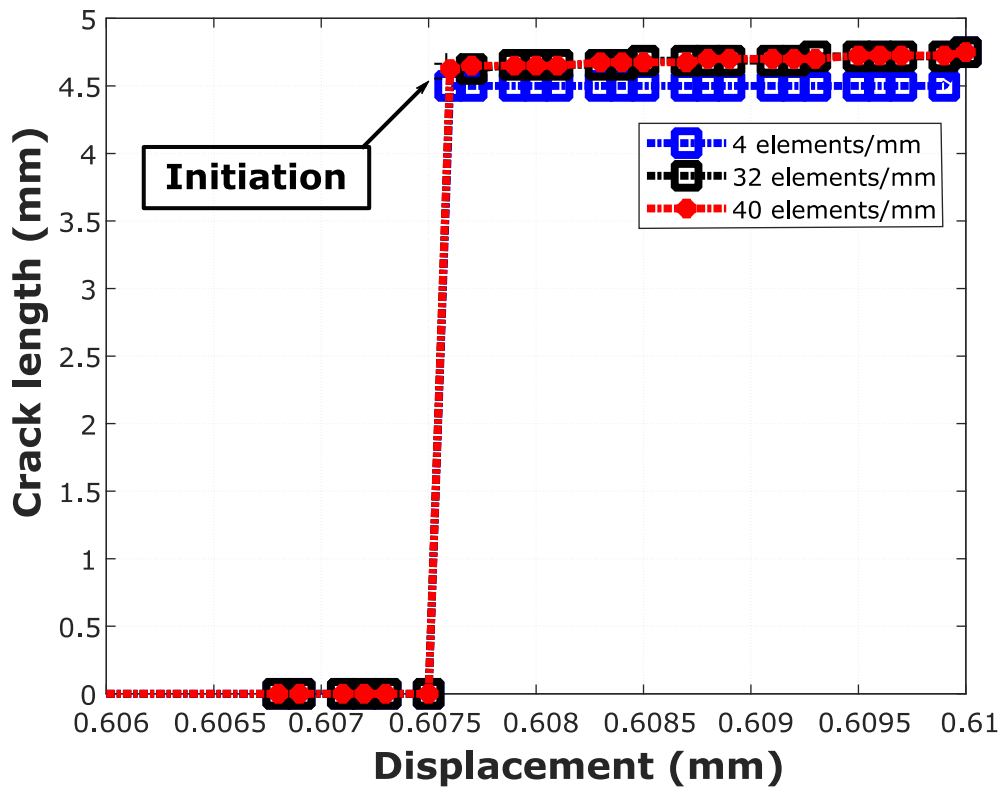


Figure 21. Interface cracking convergence for different mesh density according to the initiation criterion -  $h_s=1.62 \text{ mm}$ .

As done previously, the mesh was refined near the corner, for analyzing if the process zone was smaller than the refinement zone. Then, considering a refinement zone in the first  $6 \text{ mm}$  ( $L_{refin}=8 \text{ }\mu\text{m}$ ) of the overlap, a local study was performed near the critical load. As shown in Figure 22, a sudden initiation and propagation took place, with a quick load drop of almost  $112 \text{ N}$ . In this case, a significant length of the overlap was fully damaged,  $4.67 \text{ mm}$ , and hence the distinction of the propagation and initiation was impossible. As computed before, the choice of the method for damage parameter computation had again limitations to represent the phenomena in a mesoscale (crack initiation), even if a numerical convergence was reached.

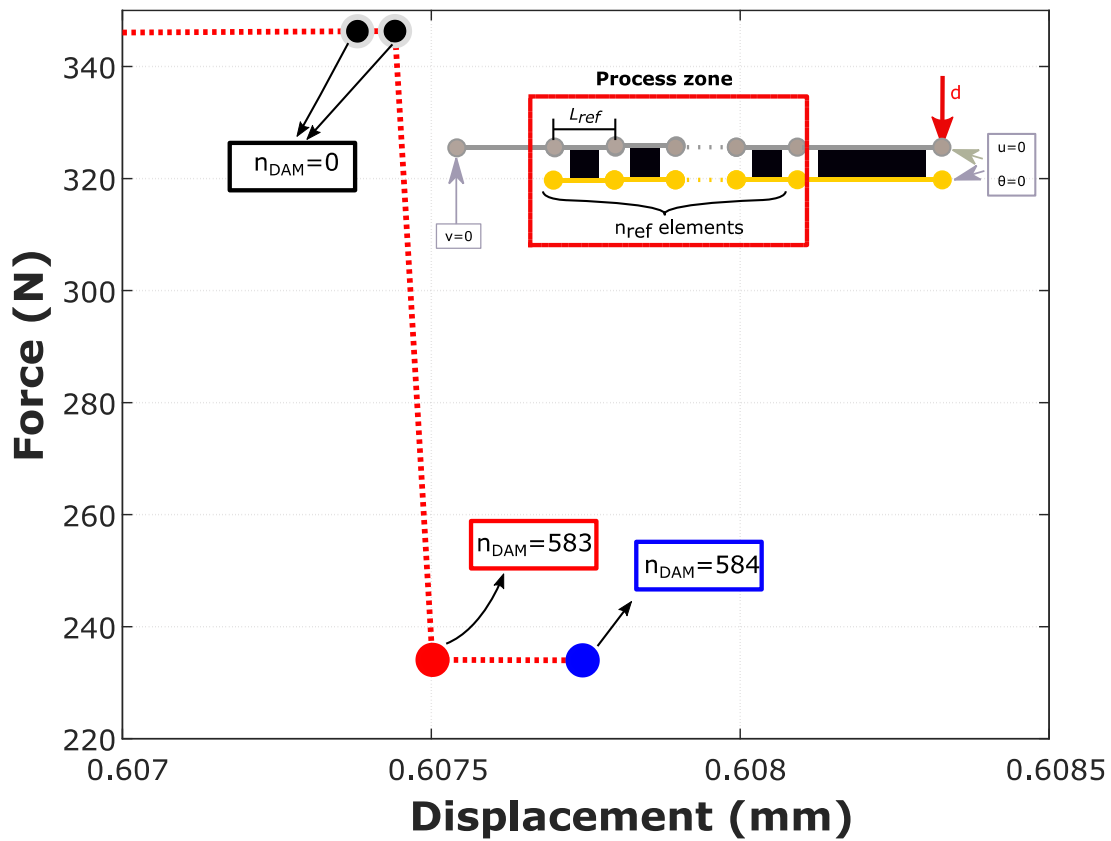


Figure 22. Zoom in the force x displacement curve (Figure 19) at the initiation of interface cracking using the refinement of  $L_{ref}=8 \mu m$ .

Finally, the global behavior after the load peak predicted that the CZM presented a progressive decrease while a sudden drop in the load was obtained experimentally. This sudden drop was related to unstable crack propagation. Hence, the particular choice of the CZM type, associated with the Newton-Raphson algorithm, could predict the maximum load, but could not be used to describe the experimental crack propagation, as similarly shown by Martin et al. (2016) [11] but on the four-point bending test.

## 6. Conclusions

In this paper, an estimation of the properties of the adhesive-to-adherend interface crack initiation, using the 3PBT and numerical analysis based on the fracture mechanics and

damage mechanics was presented. The 3PBT provides a critical load, at which an instantaneous failure takes place, and exhibits a small round zone, corresponding to the crack initiation at the interface. The study provided a more reliable proposition using the data from the 3PBT, using the CC to estimate the fracture parameters of the interface. The proposition overcame the major disadvantage of the experimental test: the properties were independent of the substrate thickness. For a fast determination of the properties, the 1D beam macro-element technique was used to estimate the energy release rate and the critical stress at fracture initiation thanks to the CC. These previous parameters were utilized to estimate the crack interface debonding using the CZM, for two different substrate thickness. The analysis was performed using a 1D beam ME technique with a bilinear damage law; the macro-results (critical force and displacement) obtained via experimental test could be estimated by a quick numerical simulation.

On the other hand, the unstable crack propagation effect could not be predicted, because of the particular choice of the CZM type, associated with the Newton-Raphson algorithm. Another limitation was the representation of a 2D fracture zone (small round surface) by an equivalent length. The influence of the fracture length played an essential role in the mesh refinement and computational time. For a small fracture length, a high mesh density was necessary, increasing the computational time. Therefore, the convergence of the crack growth indicated a threshold value of mesh density, and its increase did not result in a significant precision gain. Finally, the method assumed no mode differentiation. In the frame of the fracture of bonded joints or of the composite laminated materials, this hypothesis cannot be supported. As a result, the validity of this hypothesis should be addressed for the fracture at the adhesive-to-adherend interface.

## **Acknowledgment**

The authors gratefully acknowledge Occitanie Region and Université Fédérale de Toulouse Midi-Pyrénées for the financial support. These works were performed in the frame of the scientific network TACCOS, meaning Toulouse Adhésion Cohésion Collage Structural ( <https://personnel.isae-supaero.fr/eric-paroissien/taccos-557.html>, <http://maelenn.aufray.free.fr/taccos.php>).

## References

- [1] Hart-Smith LJ. Design methodology for bonded-bolted composite joints. Technical Report, AFWAL-TR-81-3154. Long Beach, California: Douglas Aircraft Company; 1982.
- [2] Silva LFM, Öchsner A, Adams RD. Handbook of Adhesion Technology, 2<sup>nd</sup> ed; Springer International Publishing; 2018
- [3] Kelly G .Quasi-static strength and fatigue life of hybrid (bonded/bolted) composite single-lap joints. J Compos Struct 2006; 72:119-129. <https://doi.org/10.1016/j.compstruct.2004.11.002>.
- [4] ISO 14679. Adhesives – measurement of adhesion characteristics by a three-point bending method. Geneva, Switzerland: International Organization for Standardization; 1997.
- [5] Legendre J, Créac'hcadec R, Gilbert F & Jacquet D. A new method to measure the adhesion capability of the metallic surface under shear loading using a modified Arcan test. J Adhes 2018; 94:1017-1035. <https://doi.org/10.1080/00218464.2017.1334557>.
- [6] Genty S, Sauvage JB, Tingaut P, Aufray M. Experimental and statistical study of three adherence tests for an epoxy-amine/aluminium alloy system: Pull-Off, Single Lap Joint and Three-Point Bending tests. Int J Adhes Adhes 2017; 79:50-58. <https://doi.org/10.1016/j.ijadhadh.2017.09.004>.

- [7] Roche A, Behme A, Solomon J. A three-point flexure test configuration for improved sensitivity to metal/adhesive interfacial phenomena. *Int J Adhes Adhes* 1982; 2:249–54. [https://doi.org/10.1016/0143-7496\(82\)90032-X](https://doi.org/10.1016/0143-7496(82)90032-X).
- [8] Sauvage JB, Aufray M, Jeandrau JP, Chalandon P, Poquillon D, Nardin M. Using the 3-point bending method to study failure initiation in epoxide-aluminium joints. *Int J Adhes Adhes* 2017; 75:181–189. <https://doi.org/10.1016/j.ijadhadh.2017.03.011>.
- [9] Sauvage JB, Chalandon P, Poquillon D, Nardin M, Aufray M. Using the finite element analysis method to study the 3-point bending test for the characterization of the adherence. *Int J Appli Comput Mech* 2020;6:505–516. <https://doi.org/10.22055/JACM.2019.30337.1718>.
- [10] Leguillon D. Strength or toughness? A criterion for crack onset at a notch, *Eur J Mech A-Solid* 2002; 21:61-72. [https://doi.org/10.1016/S0997-7538\(01\)01184-6](https://doi.org/10.1016/S0997-7538(01)01184-6).
- [11] Martin E, Vandellos T, Leguillon D, Carrère N. Initiation of edge debonding: coupled criterion versus cohesive zone model. *Int J Fract* 2016; 199:157–168. <https://doi.org/10.1007/s10704-016-0101-2>.
- [12] Weißgraeber P, Becker W. Finite Fracture Mechanics model for mixed mode fracture in adhesive joints. *Int J. Solids Struct* 2013; 50:2383–2394. <https://doi.org/10.1016/j.ijsolstr.2013.03.012>.
- [13] Carrère N, Martin E, Leguillon D. Comparison between models based on a coupled criterion for the prediction of the failure of adhesively bonded joints. *Eng Fract Mech* 2015; 138:185–201. <https://doi.org/10.1016/j.engfracmech.2015.03.004>.
- [14] Barenblatt GI. The formation of equilibrium cracks during brittle fracture: general ideas and hypotheses. *Axiallysymmetric Cracks PMM* 1959; 23: 622–636. [https://doi.org/10.1016/0021-8928\(59\)90157-1](https://doi.org/10.1016/0021-8928(59)90157-1).
- [15] Dugdale, D. Yielding of steel sheets containing slits. *J Mech Phys Solids* 1960; 8:100–104. [https://doi.org/10.1016/0022-5096\(60\)90013-2](https://doi.org/10.1016/0022-5096(60)90013-2).

- [16] Monteiro FJ, Barbosa MA, Gabe DR, Ross DH. Surface pretreatments of aluminium for electroplating. *Surf Coat Tech* 1988; 35:321-331. [https://doi.org/10.1016/0257-8972\(88\)90045-X](https://doi.org/10.1016/0257-8972(88)90045-X).
- [17] Lélias G, Paroissien E, Lachaud F, Morlier J, Schwartz S and Gavaille C. An extended semi-analytical formulation for fast and reliable mode I/II stress analysis of adhesively bonded joints. *Int J Solids Struct* 2015; 62:18–38. <https://doi.org/10.1016/j.ijsolstr.2014.12.027>.
- [18] Cornetti P, Mantič P, Carpinteri A. Finite Fracture Mechanics at elastic interfaces, *Int J Solids Struct* 2012; 49:1022-1032. <https://doi.org/10.1016/j.ijsolstr.2012.01.002>.
- [19] Fraisse P, Schmit F. Use of J-integral as fracture parameter in simplified analysis of bonded joints. *Int J Fracture* 1993; 63: 59–73. <https://doi.org/10.1007/BF00053316>.
- [20] Alfano G, Crisfield M: Finite element interface models for the delamination analysis of laminated composites: mechanical and computational issues. *Int J Numer Methods Engng* 2001; 50:1701–1736. <https://doi.org/10.1002/nme.93>.